



## Beam-induced surface modifications as a critical source of heat loads in the Large Hadron Collider

Valentine Petit <sup>1</sup>✉, Mauro Taborelli<sup>1</sup>, Danilo Andrea Zanin<sup>1</sup>, Marcel Himmerlich <sup>1</sup>, Holger Neupert<sup>1</sup>, Paolo Chiggiato<sup>1</sup> & Giovanni Iadarola<sup>1</sup>

Beam-induced heat loads on the cryogenic regions of the Large Hadron Collider (LHC) exhibit a wide and unexpected dispersion along the accelerator, with potential impact on the performance of its High-Luminosity upgrade. Studies related the heat load source to the avalanche multiplication of electrons at the surface of the beam vacuum chamber, a phenomenon known as electron cloud build-up. Here, we demonstrate that the topmost copper surface of beam pipes extracted from a low heat load region of the LHC consists of native  $\text{Cu}_2\text{O}$ , while the pipe surface from a high heat load region had been oxidized to  $\text{CuO}$  during LHC operation and maintenance cycles. Experiments show that this process increases the secondary electron yield and inhibits efficient surface conditioning, thus enhancing the electron cloud intensity during LHC operation. This study relates the abnormal LHC heat loads to beam-induced surface modifications of its beam pipes, enabling the development of curative solutions to overcome this critical limitation.

<sup>1</sup>European Organization for Nuclear Research, CERN, Geneva, Switzerland. ✉email: [valentine.petit@cern.ch](mailto:valentine.petit@cern.ch)

Electron clouds developing in modern particle accelerators<sup>1,2</sup> and resulting from the exponential multiplication of electrons in the vacuum beam pipe<sup>3</sup> have been identified as a critical source of beam instabilities<sup>4,5</sup>, pressure rises<sup>6,7</sup>, and heat load on the cryogenic system<sup>8,9</sup> of the Large Hadron Collider (LHC) at CERN. Different strategies have thus been implemented to mitigate the electron cloud build-up. Along room temperature parts of the LHC ring, the beam pipe surface is coated with a Non-Evaporable Getter thin film<sup>10</sup>, which exhibits a low secondary electron yield (SEY, governing the multiplication of the electrons in the beam pipe) after activation<sup>11</sup>. In the cryogenic arcs hosting the superconducting magnets, the mitigation of the electron cloud relies on beam scrubbing<sup>12</sup>, i.e., on the conditioning of the copper beam pipe surface by electrons from the cloud itself. Indeed, it has been shown that the electron irradiation of air-exposed copper leads to a SEY decrease driven by surface cleaning through electron stimulated desorption and graphitization of the airborne carbon layer<sup>13–19</sup>.

Throughout the LHC Run 1 (2010–2013), a clear reduction of the cloud-related effects has been observed<sup>20,21</sup>, proving the efficiency of the mitigation approach. The venting of the machine during the Long Shutdown 1 (2013–2015) for maintenance reactivated the electron cloud at the beginning of Run 2 in 2015 and new scrubbing was required<sup>20–22</sup>. However, since 2015, the beam-induced heat load deposited on the cryogenic system of the LHC arcs has presented some new and unexpected features. The average heat load varies up to a factor of three between the eight 2.8 km-long LHC arcs<sup>23</sup> in spite of their identical design, and by a factor up to about 13 between adjacent and nominally identical dipole magnets<sup>24</sup>. The presence of high heat load regions persisted all along Run 2 (2015–2018) despite years of accumulated scrubbing. Unfortunately, in some sections of the LHC ring, the heat load at nominal beam intensity is currently close to the cooling capacity of the cryogenic system, i.e., the cryogenic system can still maintain the nominal operating temperatures by dissipating the beam-induced heat loads, but only with little margins left. This situation could thus induce significant constraints on the operation with the increased heat load foreseen for the High-Luminosity phase of the LHC (HL-LHC), starting in 2027<sup>25,26</sup>. In the absence of a curative solution, any further increase of the heat load after the Long Shutdown 2 (2019–2021) would limit the beam intensity in the HL-LHC, with a direct detrimental impact on its attainable integrated luminosity<sup>26</sup>.

Several sources of beam-induced heat loads have been considered as a possible cause for this anomaly, such as electron cloud, synchrotron radiation, beam impedance, and beam losses. However, all of them but electron cloud could be discarded<sup>23</sup>. In addition, the observed heat load scattering corresponds well to the one obtained from electron cloud build-up simulations, assuming different SEY in the different parts of the LHC ring, as confirmed by independent measurements with different beam configurations<sup>23,27</sup>. Under this hypothesis, the heat load spread reflects a strong dispersion of electron cloud intensity along the ring, possibly due to a modification of the surface properties of some beam pipes and in particular of their SEY. This work aims to assess this hypothesis, as a first step in solving this critical issue.

During the LHC Long Shutdown 2, several cryo-dipoles, presenting different heat loads, were extracted from the ring. After venting of the corresponding sections, the beam-exposed vacuum components of a low and a high heat load dipole were extracted from their 15.5 m-long magnets according to a specific procedure to limit their deconditioning<sup>28</sup>. In the present work, the chemistry, the secondary electron yield, and the conditioning behaviour at room temperature of their beam-exposed copper surface are characterized in the laboratory. Differences between surfaces of the low and the high heat load dipole vacuum components are

identified and clearly related to their respective conditioning performance. The characteristic features of each surface are also examined within the context of existing knowledge on copper conditioning and deconditioning mechanisms<sup>13,16–19,28,29</sup>. Possible origins of these differences are then discussed, and curative solutions are considered.

## Results

**Selection of LHC dipoles and beam screen extraction.** The dipole magnet located at the LHC position B31L2 (see Supplementary Note 1 and Supplementary Fig. 1 for the naming convention of the LHC positions) was selected as the high heat load magnet for this study, since it exhibits a heat load of 60 W with two circulating beams, during a typical LHC physics fill. In parallel, the dipole located at the position C21R6 (see Supplementary Note 1) was chosen as the low heat load magnet. Even though the heat load for this individual dipole is not directly measured by sensors, the heat load of its associated half-cell (three dipoles and a quadrupole in series) is 30 W, i.e., half of that of the single B31L2 dipole magnet. The beam-induced heat load is thus significantly different for the two selected dipoles, despite a similar design and manufacturing process of their vacuum components and an identical functional position in the accelerator.

Extracting a vacuum component of a LHC dipole requires the venting of the corresponding LHC arc. Partial deconditioning of the beam exposed surfaces, i.e., an alteration of their in situ conditioning state via surface adsorption and reaction processes, is thus expected and unavoidable<sup>28</sup>. However, based on a deconditioning study<sup>28</sup>, a specific strategy was implemented to preserve at most the surface state and ensure a comparability of the different samples in spite of the time spread of the analyses. After a warm-up of the concerned LHC arcs from cryogenic to room temperature and venting of the beam pipes to atmospheric pressure with a high-purity mixture of nitrogen-oxygen (80%–20%), the two beam lines were cut at the dipole extremities and the open ends were immediately closed with Viton<sup>®</sup>-sealed caps. The magnets were then extracted from the ring, transported to the tunnel access pit, and lifted to a facility on ground level.

A schematic profile of one LHC cryo-dipole beam vacuum system is shown in Fig. 1a. The cold bore, surrounded by the superconducting coil, is maintained at 1.9 K during operations. To intercept the beam-induced heat loads due to synchrotron

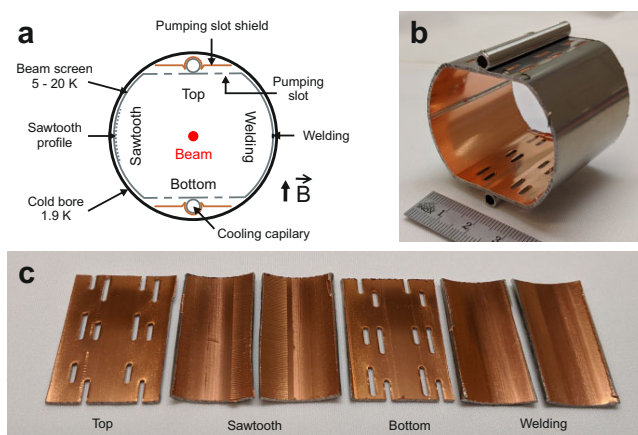


**Fig. 1** LHC beam screen. **a** Schematic of the beam vacuum system in the LHC arcs with the orientation of the dipole magnetic field  $B$ , **b** beam screen section collected for laboratory analysis, before, and **c** after cutting for fitting into the experimental set-up. The identification name of the different beam screen sides is indicated in **(a, c)**, where the welding side refers to the full lateral side and not only to the welding itself.

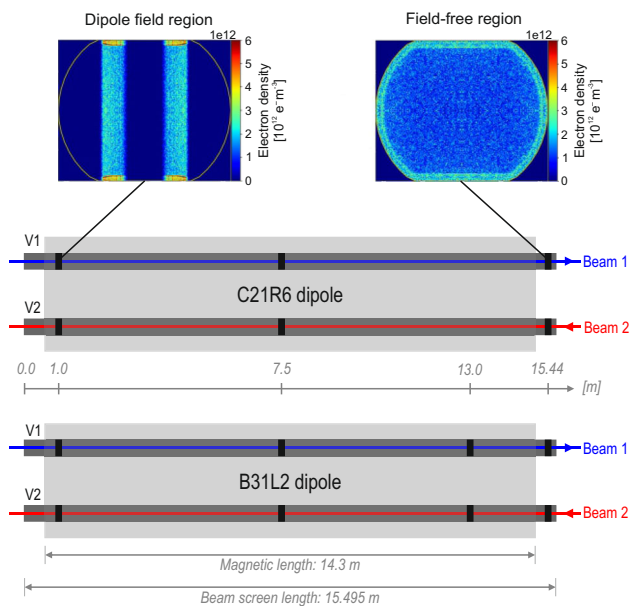


**Fig. 2** Beam screen sampling positions. Positions of the beam screen sections cut for analysis (black stripes) for Low Heat Load C21R6 and High Heat Load B31L2 LHC dipoles, and simulated electron cloud density distributions in the field and field-free regions.

radiation, impedance, and electron cloud effects, a beam screen<sup>7,8,12</sup> (co-laminated copper on stainless steel) operating between 5 and 20 K is inserted into the cold bore.

For this study, the beam screens of each magnet, referred to as High Heat Load (B31L2) and Low Heat Load (C21R6) beam screens, respectively, were collected. For each beam aperture (named V1 and V2, respectively, see Fig. 2), 5 cm-long beam screen sections as shown in Fig. 1b were sampled from different longitudinal positions depicted in Fig. 2. Beam screen sections were extracted with a clean saw from regions within the dipole field and from the field-free regions of the magnet assembly, since their electron cloud spatial density distribution is different, as shown in Fig. 2. To fit into the surface analysis setup, the sections were cut again into six parts, as displayed in Fig. 1c, where the naming convention for the beam screen sides is also defined. The inner copper surface of the entire beam screens was visually inspected, and no irregularity was observed. The extraction process lasted one day and all the beam screen sections were stored in static vacuum after extraction, to stop their deconditioning<sup>28</sup> before proceeding to their analysis. The sample collection schedule was optimized so that only two weeks were required from the venting of the LHC arcs to the storage of the samples under vacuum. During this period, the surfaces have been exposed to 1 bar of dry air as the vacuum components were sealed by end caps after the venting procedure.

**Surface characterization of as-extracted samples.** Chemical analysis by X-ray photoelectron spectroscopy (XPS) and SEY measurements were performed on the copper surface of the different beam screen sections after extraction, at different azimuthal positions.

Azimuthal profiles of maximum SEY for V1 beam screens (where the proton beam 1 was circulating) of both the Low and High Heat Load dipoles are shown in Fig. 3. The grey areas show the range of maximum SEY measured on reference beam screens (spares from the stock, never installed into the LHC).

For the Low Heat Load beam screen, all the three azimuthal SEY profiles exhibit very small scattering and no specific azimuthal pattern. In particular, for sections inside the dipole field, no

systematic maximum SEY difference is observed between the flat (top and bottom) and the curved lateral (sawtooth and welding) beam screen sides (see Fig. 1) in spite of the confinement of the electron cloud by the magnetic field. The maximum SEY value is in average between 1.6 and 1.8, i.e., significantly lower than for the spare beam screens. The same holds for the field-free region.

For beam screen sections in the field region of the High Heat Load dipole, a trend appears, beyond the larger scattering of the data. On the flat sides, the maximum SEY lies between 1.8 and 2.0, which is significantly higher than for the Low Heat Load beam screen case. On the lateral sides, the maximum SEY is found between 1.6 and 1.8, close to the values measured on the Low Heat Load beam screen samples. The beam screen section in the field-free region of the High Heat Load magnet exhibits a globally flat SEY profile, between 1.8 and 2.0, i.e., at the SEY level of the flat sections in the field region of this magnet. Similar observations were made for the V2 beam screens from each dipole, in which the second proton beam was circulating in opposite direction.

The SEY curves of the central top point (azimuthal position  $\approx 0^\circ$ ) of two beam screen sections in the field region of the High and Low Heat Load dipoles, as well as the one for a lateral side of the High Heat Load beam screen—in field—are shown in Fig. 4.

The Low Heat Load beam screen sample—top side—exhibits both a lower maximum SEY and a lower energy of the maximum SEY than the top side of the High Heat Load beam screen. The energy of the first cross-over to SEY > 1 is similar in all cases. The curve of the lateral side of the High Heat Load beam screen section and one of the flat sides of the Low Heat Load beam screen have a similar shape, even though the SEY of the latter is slightly higher.

Surface chemical analysis of the beam screens by XPS revealed the presence of carbon, oxygen, copper, as well as nitrogen and traces below 1 atomic percent (at.%) of sulfur and silicon, originating from the detergent used for the cleaning of the beam screens for UHV compatibility<sup>30</sup>.

Photoelectron and X-ray-induced Auger lines of the top sides in the dipole field of the High and Low Heat Load dipoles are shown in Fig. 5. The corresponding survey spectra are displayed in Supplementary Fig. 2 in Supplementary Note 2. The Cu 2p, O 1s, and Cu LMM Auger lines of the Low Heat Load sample are at 932.5, 530.5, and 916.7 eV respectively, indicating that copper is dominantly in Cu<sub>2</sub>O form<sup>31,32</sup>. The presence of a satellite between 939 and 947 eV on the Cu 2p line, and of a high energy shoulder on the O 1s and Cu 2p<sub>3/2</sub> states are ascribed to the presence of copper hydroxide<sup>31,32</sup>. The comparison of spectra acquired at normal, and 60° emission angle confirmed that the hydroxide layer is at the outermost surface, i.e., covering the copper oxide. The core-level line shapes are significantly different for the High Heat Load sample. The characteristic shape of the Cu 2p line satellite and the positions of the Cu 2p, O 1s, and Cu LMM lines at 933.5, 529.7, and 917.7 eV, respectively, clearly demonstrate that copper exists dominantly in CuO form<sup>31</sup>. The component at about 531.2 eV in the O 1s spectrum is ascribed to the presence of hydroxyl groups<sup>32</sup>, even though the strongly CuO-dominated shape of the Cu 2p satellite does not enable to confirm the presence of Cu(OH)<sub>2</sub>. For both the High and Low Heat Load samples, the C 1s line has its maximum at 284.7 eV, which is compatible with a graphitized carbon layer shortly exposed to air<sup>16,28</sup>. In addition, a carbon concentration of 23.5 at.% is present at the surface of this Low Heat Load sample (30.2 at.% of oxygen and 43.5 at.% of copper), while the carbon content is as low as 10.7 at.% for the High Heat Load sample (39.6 at.% of oxygen and 48.3 at.% of copper).

An azimuthally-resolved view of the oxidation state of the beam screens and its dependence on the dipole field configuration

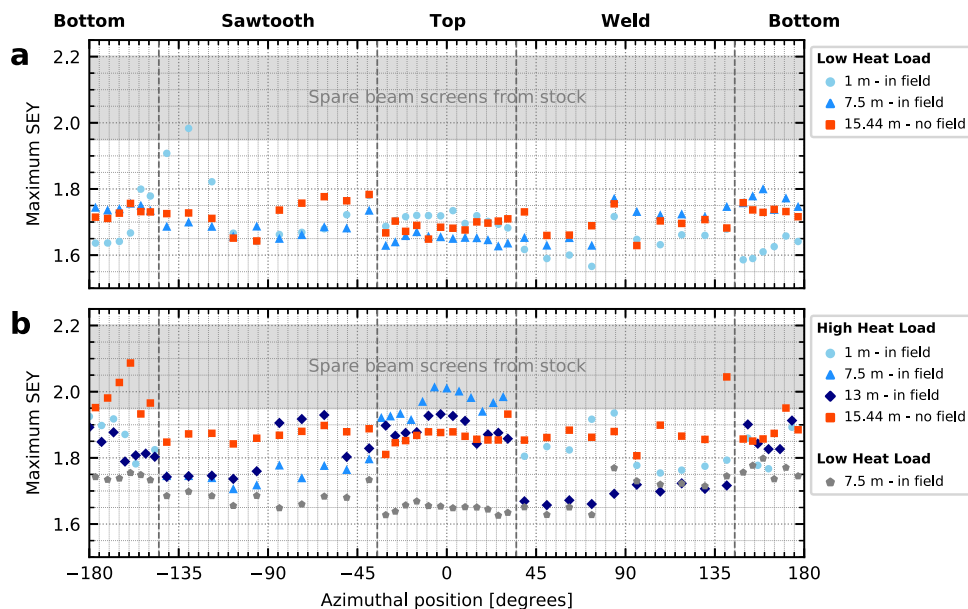


**Fig. 3** Azimuthal profiles of maximum secondary electron yield (SEY). Maximum SEY as a function of the azimuthal position for sections at different longitudinal positions represented by the different colours (see Fig. 2) along V1 beam screens from **a** Low Heat Load and **b** High Heat Load LHC dipoles, collected both in field and field-free regions. In **(b)**, a maximum SEY profile from Low Heat Load beam screen is added for comparison. The range of maximum SEY measured on spare beam screens from the stock is indicated by the grey background as a reference.

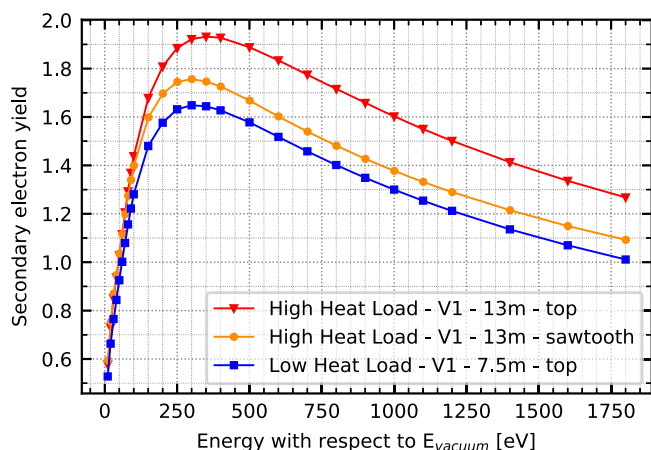


**Fig. 4** Secondary electron yield (SEY) curves. SEY curves of the top side of beam screen sections in the field region of V1 beam screens from High Heat Load (red) and Low Heat Load (blue) LHC dipoles and sawtooth side of High Heat Load beam screen (orange).

is obtained by a Wagner plot including all the XPS data acquired on the extracted beam screens. Indeed, displaying the kinetic energy of the X-ray induced Cu LMM line as a function of the binding energy of the Cu  $2p_{3/2}$  line allows to distinguish between various copper compounds, in particular between CuO, Cu<sub>2</sub>O, and Cu(OH)<sub>2</sub><sup>33</sup>. Wagner plots are typically used for pure compounds, where a single chemical component with its pure XPS chemical shift appears. In the present case, the surfaces often exhibit mixtures of different copper oxidation products, whose presence results in an additional shoulder on the lines rather than in a pure chemical shift. To account for this aspect, a Wagner-like plot was created by computing the position of the centre of gravity of the area below the Cu  $2p_{3/2}$  line between 927 and 938.5 eV and using this energy instead of the usual energy position of the maximum intensity. The resulting plots are shown in Fig. 6. The data points corresponding to pure CuO ( $E_k = 917.9$  eV and  $E_b = 934.2$  eV) and Cu<sub>2</sub>O ( $E_k = 916.9$  eV

and  $E_b = 932.7$  eV) samples are shown for reference. For clarity, only the direction of the pure Cu(OH)<sub>2</sub> position ( $E_k = 916.5$  eV and  $E_b = 934.8$  eV) is displayed, since its position is far outside the current scale.

From the distribution of the data points in Fig. 6a, b, it appears that all the sections from the Low Heat Load beam screens are uniform in the longitudinal direction, uniform in azimuth (circle and crosses are grouped), and exhibit Cu<sub>2</sub>O slightly covered by Cu(OH)<sub>2</sub>. The only exception is the V2 field-free section, which exhibits more hydroxide than other sections.

In the field region of the High Heat Load dipole (Fig. 6c), two families of points appear, corresponding to different locations on the beam screen. The data points corresponding to the lateral beam screen sides (crosses) are located in the same plot region as for the Low Heat Load beam screens, i.e., copper is mainly present in form of Cu<sub>2</sub>O, with a thin top layer of hydroxide. Instead, the data points acquired on the flat beam screen part (circles) are found closer to the CuO region of the plot. CuO thus appears to be the dominant copper oxide on these flat sides. The scattering of the data points for the flat sides does not correlate with the longitudinal position of the corresponding sections along the magnet. Fitting Cu  $2p_{3/2}$  lines acquired on the flat sides (see example in Supplementary Fig. 3 in Supplementary Note 3) allows to calculate the fraction of Cu present in the form of CuO<sup>31</sup>. The fraction of CuO was thus calculated to extend between 69 and 94% among the flat sides of the different samples. XPS spectra acquired at 60° emission angle on samples in an intermediate position between CuO and Cu<sub>2</sub>O in the Wagner-like plot showed that CuO is the top-most oxide. In the field-free part of the beam screens, the distinction between flat and lateral beam screen sides is no longer observed in the Wagner-like plot for the High Heat Load samples: CuO is found at all azimuths.

Therefore, from this Wagner-like plot, both a systematic difference of copper oxidation product between the Low and High Heat Load beam screens, and a systematic field-related distribution of CuO are confirmed for a large number of spectra.

Over all the spectra acquired in this study, the Low Heat Load samples show on average 50% more carbon than the High Heat

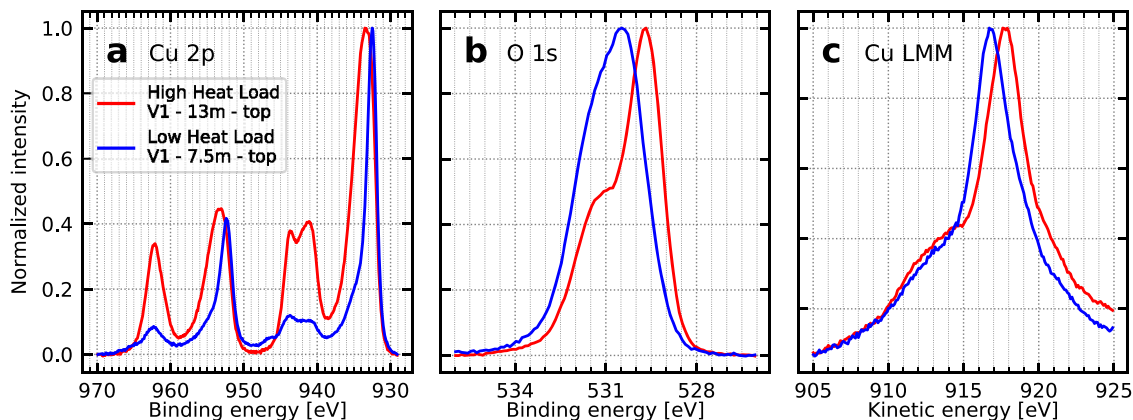


**Fig. 5 Surface chemistry of beam screens as extracted.** X-ray photoelectron spectroscopy (XPS) core level spectra of **a** Cu 2p, **b** O 1s, and **c** Cu LMM excitations for the top sides of V1 beam screen sections in the field region of the High (red) and Low (blue) Heat Load dipoles. The intensity of the spectra is normalized to its maximum, after background subtraction.

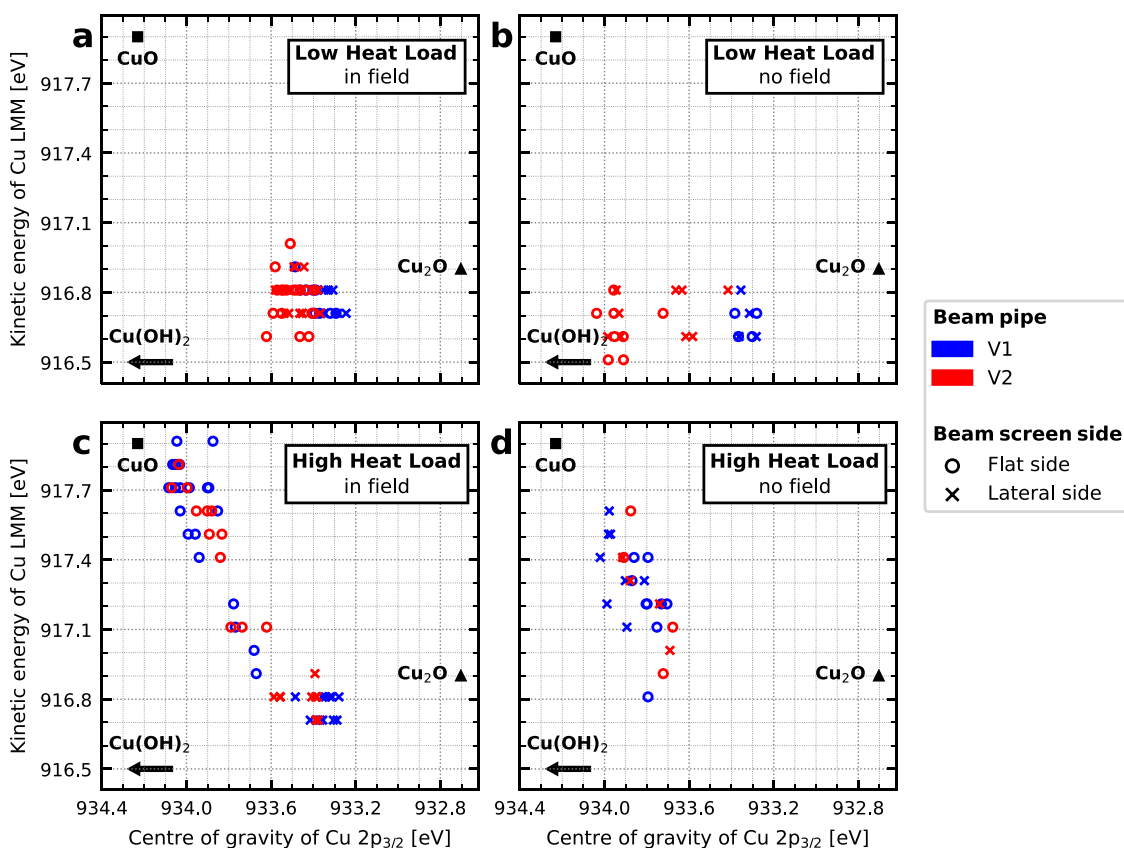


**Fig. 6 Systematic identification of copper oxidation products.** Wagner-like plots, considering the position of the Cu 2p<sub>3/2</sub> peak centre of gravity instead of intensity maximum, for all X-ray photoelectron spectroscopy (XPS) spectra acquired on the beam screens from **a, b** Low Heat Load and **c, d** High Heat Load LHC dipoles, **a–c** in field and **b–d** field-free regions. The data points corresponding to V1 beam screens are represented in blue, while the ones of V2 beam screens are plotted in red. Data acquired on the flat sides of the beam screens are represented by circles and crosses are used for data acquired on the lateral beam screen sides. The data points for reference spectra (pure compounds) are shown in black for comparison.

Load samples. No significant difference in carbon content was detected between the different sides of the beam screens, even in the field region of the dipoles.

**Laboratory experiments of electron conditioning.** All types of surfaces were conditioned, i.e., exposed to an electron flux at 250 eV in the room-temperature laboratory setup, to assess whether the observed difference in surface chemical properties impacts the conditioning kinetics and the associated surface chemical

modifications. In addition, a reference spare beam screen sample, which had never been installed in the LHC, was characterized for comparison. The conditioning curves of the bottom and welding sides of a beam screen section from the High Heat Load dipole, of the top side of a beam screen section from the Low Heat Load dipole, both located in the field region of their respective magnet and of a reference beam screen are shown in Fig. 7.

As already observed, the SEY after extraction of the CuO-free Low Heat Load beam screen sample (dose for SEY measurement = 1.6 ×

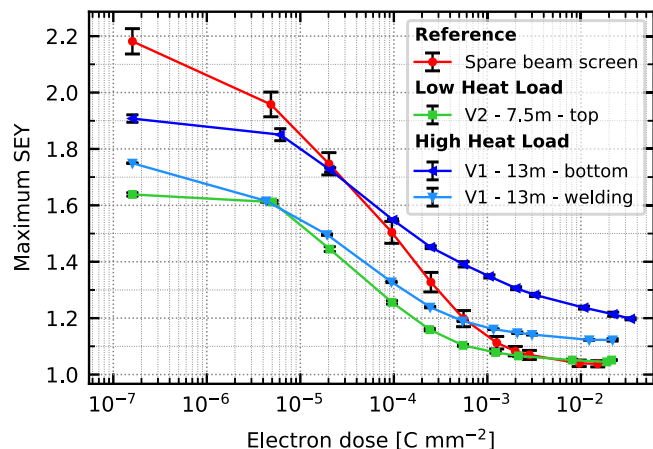


**Fig. 7 Conditioning curves.** Electron-irradiation-induced variation of the maximum secondary electron yield (SEY) of the bottom (dark blue) and welding (cyan) sides of a beam screen section from the High Heat Load dipole and of the top side of a beam screen section from the Low Heat Load dipole and of the top side of a beam screen section from the Low Heat Load dipole, all located in the field region of their respective magnet. The conditioning curve of a reference spare beam screen is given in red for comparison. The error bars represent the statistical measurement uncertainties for a confidence level of 68.3% based on three measurements performed in different locations of the samples.

$10^{-7} \text{ C mm}^{-2}$ ) is lower than for the reference beam screen and remains so up to a dose of  $2 \times 10^{-3} \text{ C mm}^{-2}$ . The ultimate SEY, i.e., the maximum SEY at saturation of the conditioning and the dose required to reach it are identical for the reference and the sample from the Low Heat Load beam screen. In particular, the ultimate SEY is well below the calculated SEY threshold of 1.25 for electron cloud build-up in the LHC arc dipoles<sup>26,34</sup>. The bottom part of the CuO-rich High Heat Load beam screen section exhibits a higher SEY directly after extraction and the subsequent decrease of the SEY is different. Indeed, no saturation of the decrease is observed, even for doses as high as  $3 \times 10^{-2} \text{ C mm}^{-2}$ , i.e., three times the dose required to reach the ultimate SEY on a reference beam screen. After such a dose, the maximum SEY remains significantly above the ultimate ones of the Low Heat Load beam screen and reference samples. This different conditioning behaviour was consistently observed for several flat beam screen sides at various locations in the field region of the High and Low Heat Load dipoles. In contrast, the conditioning of the CuO-free lateral side of the same High Heat Load beam screen section is similar to the reference and Low Heat Load sample ones. A saturation of the SEY decrease is observed for a dose of  $10^{-2} \text{ C mm}^{-2}$ . The ultimate SEY is above the one reached for the Low Heat Load beam screen and reference samples but is well below the electron cloud build-up threshold of 1.25.

Cu 2p, O 1s, and C 1s spectra for the three different beam screen surfaces are shown in Fig. 8, for different electron doses during conditioning. The corresponding survey spectra of the LHC extracted samples before and after conditioning are shown in Supplementary Fig. 4 in Supplementary Note 4. For the Low Heat Load beam screen sample, the Cu 2p satellite, the high energy shoulder of the Cu 2p<sub>3/2</sub> excitation, and the contribution in the O 1s line at around 531.5 eV all vanish as a result of the reduction of compounds from Cu(II) to lower oxidation state. After full conditioning, the Cu 2p line is similar for the Low Heat Load beam screen and reference samples. As expected<sup>16</sup>, a shift of the C 1s line of the Low Heat Load beam screen surface from 284.7 to 284.4 eV is observed during conditioning and the contribution at about 288.5 eV vanishes, indicating surface graphitization. For the bottom side of the High Heat Load beam screen, the intensity of the

CuO-related satellite and of the high energy shoulder on the Cu 2p<sub>2/3</sub> line both decrease, indicating a reduction of CuO during electron bombardment. This is also coherently reflected in the O 1s line, where a small shift of the maximum intensity occurs towards higher binding energies. However, the Cu 2p satellite is still clearly present after a dose of  $3 \times 10^{-2} \text{ C mm}^{-2}$  and the binding energy of the O 1s line (529.9 eV) remains lower than expected for Cu<sub>2</sub>O<sup>32</sup>. The reduction of the CuO layer is thus not fully completed under these experimental conditions. In parallel, even if a shift from 284.7 to 284.5 eV of the C 1s line is observed during irradiation, the contribution at 288.5 eV persists after irradiation, by opposition to the processes that occur for reference and Low Heat Load beam screen samples. For the welding side, the electron irradiation leads to the complete reduction of Cu(II) to Cu(I), as evident by the absence of the corresponding satellite line in the Cu 2p spectrum and the O 1s peak position at 530.5 eV after full conditioning (dose of  $10^{-2} \text{ C mm}^{-2}$ ). A shift of the C 1s line from 284.7 to 284.5 eV is also observed and, as for the CuO-covered bottom side, the C 1s component at 288.5 eV is still present after conditioning.

## Discussion

Two major differences in surface composition have been identified between the beam screens from the Low and the High Heat Load LHC dipoles. The first one concerns the copper oxidation state of the surfaces. A summary of the dominant copper oxidation products for the different beam screens and field configurations is given in Fig. 9 together with the electron cloud density distributions obtained from simulations.

The dominant copper oxidation product in the Low Heat Load beam screen is Cu<sub>2</sub>O, the native room-temperature copper surface oxide<sup>35</sup>. A weak signal associated with hydroxide was also observed by XPS and can be associated with the air exposure of the beam screens during extraction<sup>28</sup>. This hydroxide signal is weaker than for a non-conditioned surface<sup>16,28</sup>. It confirms a clear beam-induced conditioning effect and the effective mitigation of the deconditioning by the extraction procedure. Only one beam screen exhibits significantly more hydroxide at its extremity, which is a place more prone to contamination during the extraction phase (i.e., when opening the beam lines). The Low Heat Load beam screens are uniform in azimuth, independently of the field and electron cloud density distribution. By opposition, the beam screens from the High Heat Load dipole exhibit cupric oxide CuO, which is not observed on air-exposed reference copper surfaces neither before nor during conditioning at room temperature nor during subsequent deconditioning<sup>16,28</sup>. From Fig. 6, it appears that some XPS spectra acquired from these beam screens are quasi-identical to the one of pure bulk CuO. Assuming a mean-free path  $\lambda$  of Cu 2p photoelectrons of 1.2 nm in CuO<sup>36</sup>, the thickness of CuO in the high heat load beam screens is at least 3.6 nm (considering  $3\lambda$ , i.e., 95% of the XPS signal). Furthermore, the oxidation state of the High Heat Load beam screens shows a field-related azimuthal distribution, which corresponds perfectly to the simulated electron cloud density distribution: CuO is present where the density of impinging electrons is the greatest. It should be mentioned that the CuO-rich areas are also the ones where the energy of the impinging electrons is the highest due to the beam screen geometry and the orientation of the magnetic field. In addition to a particular oxidation state, the High Heat Load beam screens also present a very low carbon coverage, well below the one of the Low Heat Load beam screens. In particular, the surface cleanliness of some High Heat Load beam screen samples is unachievable by the detergent cleaning process applied to the beam screens prior to their installation in the LHC. Based on these observations, it is

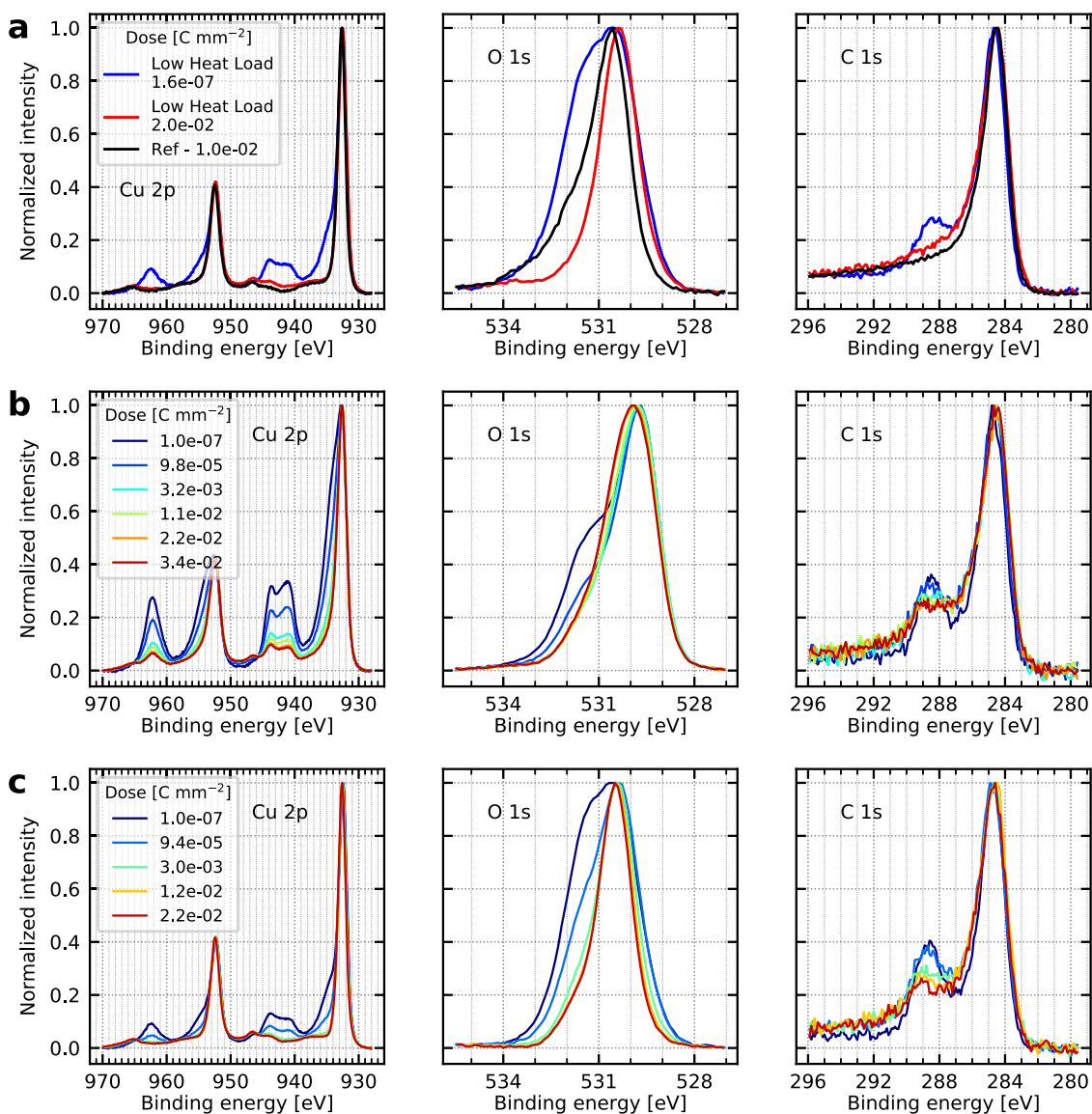


**Fig. 8 Surface chemistry during conditioning.** Cu 2p, O 1s, and C 1s X-ray photoelectron spectroscopy (XPS) core level spectra at a different dose (represented by the corresponding colours) during conditioning of **a** the Low Heat Load sample and the reference sample, **b** the High Heat Load bottom sample, and **c** the High Heat Load lateral side sample.

concluded that LHC beam operation is an essential—but not unique—factor for both, the formation of CuO and the low carbon surface concentration.

These two major differences in the surface chemical composition of the beam screens from the two dipoles have consequences on LHC performance. Even after short exposure to ambient conditions, the  $\text{Cu}_2\text{O}$ -dominated regions show a maximum SEY between 1.6 and 1.8, which remains lower than the SEY of air-exposed copper, proving again a clear beam-induced conditioning effect. By opposition, the CuO-rich regions exhibit a higher SEY, between 1.8 and 2.0. Thus, the presence of CuO favours the electron cloud build-up compared to  $\text{Cu}_2\text{O}$ . A further evidence of a worse performance of the CuO-rich surfaces is their delayed and less effective conditioning at room temperature in the laboratory. The conditioning at room temperature of CuO-rich samples relies on the partial reduction of CuO to  $\text{Cu}_2\text{O}$ . Such a reduction under electron bombardment at room temperature has already been observed<sup>37,38</sup>. However, it has been demonstrated that this reduction is strongly hindered at 180 K due to the slower diffusion of copper and oxygen atoms<sup>37</sup>. An even slower

or inhibited conditioning is thus expected at the operation temperature of the LHC beam screens (5–20 K). This hypothesis is compatible with the presence of CuO observed in the High Heat Load beam screens even after years of accumulated scrubbing. A dedicated laboratory setup is currently under construction to perform conditioning coupled with XPS analyses of Low and High Heat Load beam screen samples at about 10 K and to investigate these aspects in greater detail. Moreover, the low carbon amounts observed on the high heat load beam screens as extracted from the ring also affect the conditioning, since the presence of carbon to be graphitized is necessary to decrease the maximum SEY of air-exposed copper down to about 1.1 during electron irradiation<sup>16</sup>. A low carbon amount translates into a low in situ graphitic coverage of the surface, and thus a limited SEY reduction by electron cloud bombardment. This could thus be the reason why the CuO-free lateral side of High Heat Load beam screen has a higher ultimate SEY than the CuO-free Low Heat Load flat beam screen side in Fig. 7. Furthermore, carbon was shown to assist in the reduction of underlying CuO oxide, by allowing an oxygen transfer from copper to carbon<sup>37,39</sup>.

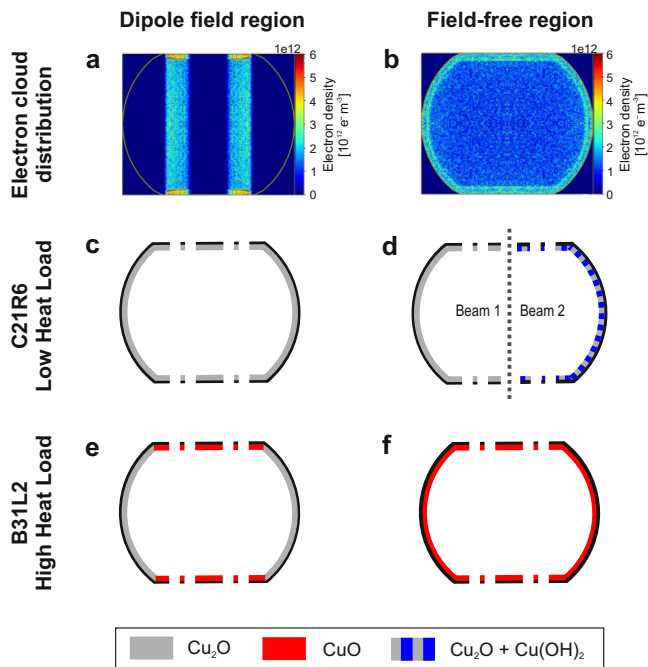


**Fig. 9 Summary of copper oxidation state.** **a, b** Summary of the electron cloud density distributions obtained from simulations; schematic of the distribution of the different main copper oxidation products found on the beam screens of **c, d** the Low and **e, f** the High Heat Load LHC dipoles and their dependence on the magnetic field.

Consequently, a low initial surface carbon content is also not favouring in situ CuO reduction via electron bombardment. Based on these observations, both the presence of CuO and the low carbon coverage of some beam screens are currently considered as likely responsible for the observed high beam-induced heat load in some sections of the LHC ring.

Since cupric oxide CuO is not observed at any step of the copper conditioning and deconditioning experiments at room temperature in the laboratory<sup>16,28</sup>, the CuO build-up observed in some LHC beam screens should be related to a difference of experimental conditions between the laboratory and LHC environments, in particular to the difference in temperature.

To understand CuO build-up mechanisms in the LHC, different sources of oxygen are considered. The first one is the residual gas in the beam vacuum system itself. The fact that CuO is not observed on the lateral sides of the high heat load beam screens in the field region implies that CuO is not formed by radicals moving around as neutrals produced by the electron cloud or the beam. CuO can be produced by bombardment of copper surfaces by oxygen ions at cryogenic temperature<sup>40</sup>. The presence of such ions in the beam vacuum system of the LHC is plausible. However, the residual gas density is too low to explain the build-up of at least 2 nm of CuO within the operation time of the LHC, as demonstrated in Supplementary Note 5. CuO build-up from any residual gas being adsorbed on the beam screen surface is also excluded. Indeed, before cool-down of the machine, the beam vacuum system is evacuated to  $10^{-4}$  mbar. In the assumption that all this residual gas is water (unbaked system) and is being condensed on the inner surface of the beam screens during cool-down leads to an additional surface coverage of 0.01 monolayer of water, which is too low to explain the observed CuO amount. The residual gas density after cool-down and during beam operation is even lower by orders of magnitude and is therefore not a significant source for gas adsorption on the beam screen surface.

Another source of oxygen is the one already present on the surface due to air exposure. Hydroxide, which spontaneously grows on an air-exposed copper surface<sup>32,41</sup>, was certainly present on the beam screen surface at the restart of the LHC after the Long Shutdown 1. Electron irradiation of bulk Cu(OH)<sub>2</sub> generates CuO on the surface<sup>42</sup>. However, at room temperature, airborne Cu(OH)<sub>2</sub> was reduced to Cu<sub>2</sub>O upon electron bombardment<sup>43</sup>. This difference compared to electron irradiation of bulk Cu(OH)<sub>2</sub> indicates that the underlying substrate and diffusion phenomena play a crucial role in the surface reduction to Cu<sub>2</sub>O. Under this hypothesis, electron irradiation of airborne Cu(OH)<sub>2</sub> at cryogenic temperature could also result in CuO formation due to limited oxygen diffusivity. This hypothesis is compatible with the correspondence of CuO and electron cloud density distributions. Furthermore, the absence of CuO observed on the lateral sides of the High Heat Load beam screens (in their field region), where the energy of the impinging electron is lower, could also indicate an energy threshold for the conversion of Cu(OH)<sub>2</sub> into CuO. These different hypotheses will be tested in the laboratory on the cryogenic setup being currently built. If this is confirmed, the difference of heat load observed along the LHC ring could be related to a difference in the hydroxide content present at the restart of the accelerator for Run 2. CuO build-up from other adsorbed species (water present at a sub-monolayer coverage after pump-down, oxygen-containing contamination etc.) will also be investigated.

The relation between the distribution of CuO and the one of carbon is still unclear. The carbon depletion and the component on the C 1s spectrum at about 288.5 eV that persists at all azimuths after conditioning of the High Heat Load beam screens seems to indicate that, besides CuO formation, other surface reactions occur in parallel, which possibly includes the formation of mobile, reactive species, as well as volatile products, which are not influenced by the magnetic field. Understanding the origin of CuO build-up could help in turn understanding the origin of carbon depletion and the non-uniformity of the LHC heat load distribution.

Preventing any further increase of the LHC heat load during the Long Shutdown 2 is crucial since some sections of the accelerator were already operating close to the limit of the cryogenic capacity during Run 2. Under the hypothesis of CuO being responsible for the high heat load, and until the exact mechanism for its build-up in the LHC being elucidated, the strategy consists in limiting the oxygen input by re-pumping down the beam vacuum system as soon as the Long Shutdown 2 maintenance is completed.

Curative solutions against CuO are also considered and developed for a future implementation in the LHC during the Long Shutdown 3 (2025–2027). A first approach consists of reducing CuO either by thermal treatment or UV exposure, both possibly assisted by a reducing atmosphere<sup>44–48</sup> or with an atmospheric-pressure hydrogen-containing plasma<sup>49</sup>. A second option could be to etch away the CuO layer by physical etching, e.g., ion bombardment<sup>50</sup>. Finally, covering the CuO surface by injecting a carbon-rich gas followed by the beam-scrubbing of the newly adsorbed layer, or by directly applying a low-SEY carbon coating<sup>51,52</sup> will be tested. The feasibility of all these options will be evaluated in the light of the different constraints imposed by the specificities of the LHC beam vacuum system.

## Conclusions

During the Long Shutdown 2 of the LHC, the surfaces of beam screens extracted from a low and a high heat load LHC dipoles were analyzed in the laboratory. The beam screens from the low heat load dipole exhibit the usual features of an electron-



irradiated copper surface: the dominance of Cu<sub>2</sub>O copper oxide, slightly covered by Cu(OH)<sub>2</sub> and low SEY. In contrast, the beam screens from the high heat load dipole consist of a CuO-rich surface, which exhibits a field-related azimuthal distribution matching the one of the electron cloud density, as well as a low carbon coverage. The presence of CuO is demonstrated to increase the SEY of the copper surface and significantly slow down its room temperature conditioning, i.e., its SEY reduction under electron bombardment. Therefore, a direct relation between the chemical state of the LHC beam screens and their electron-cloud-related properties have been evidenced, which could explain the abnormally high heat load observed in some LHC sections.

Several hypotheses for the formation of the CuO layer and carbon depletion are under investigation. The results should enable to find the cause of the differences which developed among the nominally identical parts of the LHC ring and will give an important feedback helping to prevent a further formation of CuO and a possible increase of the heat load in different regions of the LHC.

## Methods

**Surface characterization in the laboratory.** Surface chemical analysis by XPS, SEY measurements, and conditioning tests were performed in a room temperature UHV system described in detail elsewhere<sup>16</sup>. It consists of a main vacuum chamber (base pressure  $6 \times 10^{-10}$  mbar) equipped with a monochromated Al K $\alpha$  X-ray source and a hemispherical electron energy analyzer collecting photoelectrons at normal emission angle. The energy scale is calibrated setting the Cu 2p<sub>3/2</sub> and the Au 4f<sub>7/2</sub> states of sputter-cleaned metals to 932.6 and 84.0 eV, respectively. The atomic concentrations of the present elements are obtained assuming a uniform material and weighting the respective peak area of the XPS spectrum by the corresponding sensitivity factor.

The SEY, defined as the ratio of a number of emitted electrons per number of incident electrons, is measured with a dedicated electron gun using the method of alternating sample bias<sup>16</sup> ( $V_{sa} = \pm 47.5$  V). The energy of the primary electrons is varied by steps from 10 to 1800 eV. The estimated dose associated with such a SEY spectrum is  $1.6 \times 10^{-7}$  C mm<sup>-2</sup>. The reproducibility of the measurement is estimated from the acquisition of two consecutive SEY curves at the same sample position to 0.01 on the maximum SEY. SEY measurements are performed before XPS analysis, to avoid any X-ray-induced conditioning effects of the surface, which could impact the SEY values.

Conditioning is carried out using a flood gun irradiating the samples at normal incidence angle with 250 eV electrons at a current density of about 140 nA mm<sup>-2</sup>. The samples were irradiated up to a dose of at least  $10^{-2}$  C mm<sup>-2</sup>, at which the SEY decrease is known to saturate for the conditioning of air-exposed copper<sup>18</sup>.

**Sample preparation.** The samples from LHC extracted beam screens were collected from the vacuum storage system just before their analysis, to limit at most their deconditioning. Samples of spare beam screens from the stock, never exposed to LHC's proton beam, were also analyzed, and conditioned for comparison. These samples have been cleaned in an alkaline detergent solution based on NGL 17.40 P. SP from NGL Cleaning Technology SA, to ensure their UHV compatibility<sup>30</sup>, as the LHC extracted beam screens analyzed in this study, prior to their installation in the accelerator.

Reference samples of CuO, Cu<sub>2</sub>O were obtained by sputtering while Cu(OH)<sub>2</sub> reference sample was produced by anodization of copper in 1M caustic soda solution.

## Data availability

The datasets generated and analyzed during the current study are available from the corresponding author on reasonable request.

Received: 18 March 2021; Accepted: 4 August 2021;

Published online: 23 August 2021

## References

- Fischer, W. et al. Electron cloud observations and cures in the Relativistic Heavy Ion Collider. *Phys. Rev. Spec. Top.—Accel. Beams* **11**, 041002 (2008).
- Suetsugu, Y. et al. Achievements and problems in the first commissioning of SuperKEKB vacuum system. *J. Vac. Sci. Technol. A* **35**, 03E103 (2017).
- Cimino, R. & Demma, T. Electron cloud in accelerators. *Int. J. Mod. Phys. A* **29**, 1430023 (2014).
- Zimmermann, F. A simulation study of electron-cloud instability and beam-induced multipacting in the LHC. <http://cds.cern.ch/record/323928> (1997).
- Romano, A., Boine-Frankenheim, O., Buffat, X., Iadarola, G. & Rumolo, G. Electron cloud buildup driving spontaneous vertical instabilities of stored beams in the Large Hadron Collider. *Phys. Rev. Accel. Beams* **21**, 61002 (2018).
- Domínguez, O. et al. First electron-cloud studies at the Large Hadron Collider. *Phys. Rev. Spec. Top.—Accel. Beams* **16**, 011003 (2013).
- Gröbner, O. Technological problems related to the cold vacuum system of the LHC. *Vacuum* **47**, 591–595 (1996).
- Gröbner, O. Overview of the LHC vacuum system. *Vacuum* **60**, 25–34 (2001).
- Rumolo, G., Ruggiero, F. & Zimmermann, F. Simulation of the electron-cloud build up and its consequences on heat load, beam stability, and diagnostics. *Phys. Rev. Spec. Top.—Accel. Beams* **4**, 012801 (2001).
- Chiggiato, P. & Costa Pinto, P. Ti-Zr-V non-evaporable getter films: From development to large scale production for the Large Hadron Collider. *Thin Solid Films* **515**, 382–388 (2006).
- Henrist, B., Hilleret, N., Scheuerlein, C. & Taborelli, M. Secondary electron yield of TiZr and TiZrV non-evaporable getter thin film coatings. *Appl. Surf. Sci.* **172**, 95–102 (2001).
- Brüning, O. et al. *LHC Design Report*. Report no. CERN-2004-003-V-1 <https://doi.org/10.5170/CERN-2004-003-V-1> (CERN, Geneva, 2004).
- Scheuerlein, C., Taborelli, M., Hilleret, N., Brown, A. & Baker, M. A. An AES study of the room temperature conditioning of technological metal surfaces by electron irradiation. *Appl. Surf. Sci.* **202**, 57–67 (2002).
- Pivi, M. T. F. et al. Experimental observations of in situ secondary electron yield reduction in the PEP-II particle accelerator beam line. *Nucl. Instrum. Methods Phys. Res. Sect. A Accel. Spectrometers, Detect. Assoc. Equip.* **621**, 47–56 (2010).
- Henrist, B., Hilleret, N., Scheuerlein, C., Taborelli, M. & Vorlauffer, G. The variation of the secondary electron yield and of the desorption yield of copper under electron bombardment: origin and impact on the conditioning of the LHC. In *Proc. 8th European Particle Conference: EPAC 2002 2553* (European Physical Society, Geneva, 2002).
- Petit, V., Taborelli, M., Neupert, H., Chiggiato, P. & Belhaj, M. Role of the different chemical components in the conditioning process of air exposed copper surfaces. *Phys. Rev. Accel. Beams* **22**, 083101 (2019).
- Lariciprete, R., Grosso, D. R., Comisso, M., Flammini, R. & Cimino, R. Secondary electron yield of Cu technical surfaces: dependence on electron irradiation. *Phys. Rev. Spec. Top.—Accel. Beams* **16**, 011002 (2013).
- Cimino, R. et al. Nature of the decrease of the secondary-electron yield by electron bombardment and its energy dependence. *Phys. Rev. Lett.* **109**, 064801 (2012).
- Nishiwaki, M. & Kato, S. Graphitization of inner surface of copper beam duct of KEKB positron ring. *Vacuum* **84**, 743–746 (2009).
- Rumolo, G. et al. Electron cloud effects at the CERN accelerators. In *E-CLOUD'18: Proc. Joint INFN-CERN-ARIES Workshop on Electron-Cloud Effects* (eds Cimino, R., Rumolo, G. & Zimmermann, F.) 13–19 (CERN, Geneva, 2020).
- Baglin, V. The LHC vacuum system: commissioning up to nominal luminosity. *Vacuum* **138**, 112–119 (2017).
- Yin Vallgren, C., Metidieri, P. R. & Bregliozzi, G. Beam induced dynamic pressure during Run 2 (2015–2018) machine operation in the LHC. In *E-CLOUD'18: Proc. Joint INFN-CERN-ARIES Workshop on Electron-Cloud Effects* (eds Cimino, R., Rumolo, G. & Zimmermann, F.) 65–72 (CERN, Geneva, 2020).
- Skripka, G. et al. Comparison of electron cloud build-up simulations against heat load measurements for the LHC arcs with different beam configurations. In *Proc. 10th International Particle Accelerator Conference, IPAC19 3232–3235* (Jacow, Geneva, Switzerland, 2019).
- Iadarola, G. et al. Overview of heat loads in the LHC. In *E-CLOUD'18: Proc. Joint INFN-CERN-ARIES Workshop on Electron-Cloud Effects* (eds Cimino, R., Rumolo, G. & Zimmermann, F.) 51–58 (CERN, Geneva, 2020).
- Rumolo, G. Beam dynamics challenges for the LHC and injector upgrades. In *Proc. 61st ICFABDW on High-Intensity and High-Brightness Hadron Beams 8–13* (JACoW, Geneva, 2018).
- Apollinari, G. et al. *High-Luminosity Large Hadron Collider (HL-LHC): Technical Design Report V. 0.1*. Report no. CERN-2017-007-M <https://doi.org/10.23731/CYRM-2017-004> (CERN, 2017).
- Iadarola, G. et al. *Beam-Induced Heat Loads on the LHC Arc Beam Screens with Different Beam and Machine Configurations: Experiments and Comparison Against Simulations*. Report No. CERN-ACC-2019-0057 <http://cds.cern.ch/record/2705513/files/CERN-ACC-NOTE-2019-0057.pdf> (CERN, 2019).
- Petit, V. et al. Impact of deconditioning on the secondary electron yield of Cu surfaces in particle accelerators. *Phys. Rev. Accel. Beams* **23**, 093101 (2020).
- Scheuerlein, C. & Taborelli, M. Electron stimulated carbon adsorption in ultrahigh vacuum monitored by Auger electron spectroscopy. *J. Vac. Sci. Technol. A-Vac. Surf. Film.* **20**, 93–101 (2002).

30. Scheuerlein, C. & Taborelli, M. The assessment of metal surface cleanliness by XPS. *Appl. Surf. Sci.* **252**, 4279–4288 (2006).
31. Biesinger, M. C. Advanced analysis of copper X-ray photoelectron spectra. *Surf. Interface Anal.* **49**, 1325–1334 (2017).
32. Robert, T., Bartel, M. & Offergeld, G. Characterization of oxygen species adsorbed on copper and nickel oxides by X-ray photoelectron spectroscopy. *Surf. Sci.* **33**, 123–130 (1972).
33. Wagner, C. D., Gale, L. H. & Raymond, R. H. Two-dimensional chemical state plots: a standardized data set for use in identifying chemical states by X-ray photoelectron spectroscopy. *Anal. Chem.* **51**, 466–482 (1979).
34. Skripka, G. & Iadarola, G. *Beam-Induced Heat Loads on the Beam Screens of the HL-LHC Arcs*. Report No. CERN-ACC-NOTE-2019-0041 (CERN, Geneva, 2019).
35. Chawla, S. K., Rickett, B. I., Sankarraman, N. & Payer, J. H. An X-ray photoelectron spectroscopic investigation of the air-formed film on copper. *Corros. Sci.* **33**, 1617–1631 (1992).
36. Lesiak, B., Jablonski, A., Zemek, J. & Jiricek, P. Determination of the inelastic mean free paths of electrons in copper and copper oxides by elastic peak electron spectroscopy (EPES). *Surf. Interface Anal.* **26**, 400–411 (1998).
37. Losev, A., Kostov, K. & Tyuliev, G. Electron beam induced reduction of CuO in the presence of a surface carbonaceous layer: an XPS/HREELS study. *Surf. Sci.* **213**, 564–579 (1989).
38. Long, N. J. & Petford-Long, A. K. In situ electron-beam-induced reduction of CuO: a study of phase transformations in cupric oxide. *Ultramicroscopy* **20**, 151–160 (1986).
39. Li, J. et al. Influence of carbon on the enhanced oxygen loss in copper oxide films. *Appl. Phys. Lett.* **58**, 1344–1346 (1991).
40. Usuki, N. Photoelectron spectroscopic study of copper surfaces changed by oxygen ion bombardment. *Vacuum* **41**, 1683–1685 (1990).
41. Barr, T. L. An ESCA study of the termination of the passivation of elemental metals. *J. Phys. Chem.* **82**, 1801–1810 (1978).
42. Günter, J. R. & Oswald, H. R. Topotactic electron induced and thermal decomposition of copper (II) hydroxide. *J. Appl. Crystallogr.* **3**, 21–26 (1970).
43. Petit, V. *Conditioning of Surfaces in Particle Accelerators*. ISAE-SUPAERO <https://doi.org/10.17181/CERN.941V.OBEC> (2020).
44. Rodriguez, J. A., Kim, J. Y., Hanson, J. C., Pérez, M. & Frenkel, A. I. Reduction of CuO in H<sub>2</sub>: in situ time-resolved XRD studies. *Catal. Lett.* **85**, 247–254 (2003).
45. Kim, J. Y., Rodriguez, J. A., Hanson, J. C., Frenkel, A. I. & Lee, P. L. Reduction of CuO and Cu<sub>2</sub>O with H<sub>2</sub>: H embedding and kinetic effects in the formation of suboxides. *J. Am. Chem. Soc.* **125**, 10684–10692 (2003).
46. Li, J. X. & Liu, A. H. Reduction of copper oxide induced by 172 nm vacuum ultraviolet radiation at ambient temperature. *J. Electron. Mater.* **40**, 2105–2110 (2011).
47. Fleisch, T. H. & Mains, G. J. Reduction of copper oxides by UV radiation and atomic hydrogen studied by XPS. *Appl. Surf. Sci.* **10**, 51–62 (1982).
48. Lee, S. Y., Mettlach, N., Nguyen, N., Sun, Y. M. & White, J. M. Copper oxide reduction through vacuum annealing. *Appl. Surf. Sci.* **206**, 102–109 (2003).
49. Sawada, Y., Tamaru, H., Kogoma, M., Kawase, M. & Hashimoto, K. The reduction of copper oxide thin films with hydrogen plasma generated by an atmospheric-pressure glow discharge. *J. Phys. D: Appl. Phys.* **29**, 2539–2544 (1996).
50. Panzner, G., Egert, B. & Schmidt, H. P. The stability of CuO and Cu<sub>2</sub>O surfaces during argon sputtering studied by XPS and AES. *Surf. Sci.* **151**, 400–408 (1985).
51. Yin Vallgren, C. et al. Amorphous carbon coatings for the mitigation of electron cloud in the CERN Super Proton Synchrotron. *Phys. Rev. Spec. Top.—Accel. Beams* **14**, 071001 (2011).
52. Van Gompel, M. et al. Amorphous carbon thin film coating of the SPS beamline: evaluation of the first coating implementation. In *Proc. 8th International Particle Accelerator Conference, IPAC 2017* 44–47 (JACoW, Geneva, Switzerland, 2017).

### Acknowledgements

The authors acknowledge the CERN TE-VSC and TE-MS group members involved in the extraction of the dipoles and beam screens. This study has been possible thanks to the continuous support and fruitful suggestions of the LHC Beam-Induced Heat Loads Task Force. Mohamed Belhaj (ONERA) is gratefully acknowledged for fruitful discussions.

### Author contributions

V.P., M.T. and G.I. defined the strategy and methods for the selection, extraction, and analysis of the beam screens. V.P., D.A.Z. and M.H. acquired the data with the technical support of H.N. D.A.Z. implemented the data extraction routine. V.P. and M.T. analyzed the data and interpreted the results with M.H. and P.C.

### Competing interests

The authors declare no competing interests

### Additional information

**Supplementary information** The online version contains supplementary material available at <https://doi.org/10.1038/s42005-021-00698-x>.

**Correspondence** and requests for materials should be addressed to V.P.

**Peer review information** *Communications Physics* thanks Isabel Montero and the other, anonymous, reviewer(s) for their contribution to the peer review of this work.

**Reprints and permission information** is available at <http://www.nature.com/reprints>

**Publisher's note** Springer Nature remains neutral with regard to jurisdictional claims in published maps and institutional affiliations.



**Open Access** This article is licensed under a Creative Commons Attribution 4.0 International License, which permits use, sharing, adaptation, distribution and reproduction in any medium or format, as long as you give appropriate credit to the original author(s) and the source, provide a link to the Creative Commons license, and indicate if changes were made. The images or other third party material in this article are included in the article's Creative Commons license, unless indicated otherwise in a credit line to the material. If material is not included in the article's Creative Commons license and your intended use is not permitted by statutory regulation or exceeds the permitted use, you will need to obtain permission directly from the copyright holder. To view a copy of this license, visit <http://creativecommons.org/licenses/by/4.0/>.

© The Author(s) 2021